Direct Numerical Simulation of Transition over a NLF Aerofoil: Methods and Validation

Tapan K. Sengupta[1], Yogesh G. Bhumkar[2]

Department of Aerospace Engineering, Indian

Institute of Technology Kanpur, Kanpur 208016, India

[1]tksen@iitk.ac.in; [2]bhumkaryogesh@gmail.com

Abstract

In the present study, we identify the need for high accuracy computing for capturing the transition to turbulence for the flow past a natural laminar flow aerofoil by direct numerical simulation. The major computational elements which contribute error in performing DNS have been identified here and systematically shown to be removed by appropriate grid, numerical method and post-processing tools. We have shown a better way of generating orthogonal grid around thick and cambered aerofoil which helps in significant reduction of numerical errors. DNS of SHM-1 aerofoil for $Re = 10.3 \times 10^6$ has been made possible by the use of high accuracy dispersion relation preserving compact scheme, which also has the potential to introduce aliasing error and spurious upstream propagating disturbances (q-waves). Systematic analysis of such methods helps us to use an appropriate fine grid along with upwind and multi-dimensional filters to remove these problems. The simulation results clearly identify the route of bypass transition for this flow field.

Keywords

Direct Numerical Simulation; Bypass Transition; NLF Aerofoil; Orthogonal Grid; Multi-dimensional Filters; Upwind Filter

Introduction

Performance of an aircraft can be improved by a well-designed wing. In this context, flow over an aerofoil is an important research topic in aerodynamics. The present work is focused on obtaining time accurate numerical solutions for transitional flows past a natural laminar flow (NLF) aerofoil. By definition, NLF aerofoils are designed in such a way that transition from laminar to turbulent flow is delayed on the suction surface, as far aft as possible. The process of transition begins via flow instability and in most of the design efforts of NLF aerofoils, the onset of flow instability is delayed. One of the most commonly studied and understood flow instability for wall bounded flows is the classical route associated with the formation of Tollmien-Schlichting (TS) waves.

Early researches in flow instability studies focused attention on understanding basic mechanisms for inviscid disturbance flows, with the assumption that viscous actions can only stabilize flows. This is the basis of early works of Kelvin, Helmholtz, Rayleigh and others, which can be found in *(Drazin and Reid, 1981; Sengupta, 2012)*. This could not, however, explain the flow transition over a flat plate and led to efforts which attempted to understand the role of viscous actions via the solution of Orr-Sommerfeld equation, through the researches reported in *(Heisenberg, 1924; Schlichting, 1933; Tollmien, 1931)*, where the stability of flow over a flat plate was investigated as an example of zero pressure gradient Blasius boundary layer. It is shown that if small amplitude monochromatic time harmonic disturbance is excited locally, then the response field appears as TS wave and travels in space exhibiting growth. Results in *(Schlichting, 1933; Tollmien, 1931)* predicted onset of criticality and provided properties of unstable waves, whose experimental verification came via the pioneering effort of *(Schubauer and Skramstad, 1947)*. Since then spatial growth of TS waves is thought to be responsible for flow transition with the implicit view that the primary instability eventually leads to flow transition, following other secondary and tertiary instabilities. While different frequencies suffer differential growth rates, appearance of TS wave is considered as a precursor to transition.

According to *(Morkovin, 1969)*, there are instances where flow transitions are seen to occur without the presence of TS waves and these are collectively categorized as *bypass transition*. We note that such terminology does not imply that there is only one bypass transition route. For example, one such bypass transition route has been shown theoretically and experimentally in *(Lim et al., 2004)* and *(Sengupta et al., 2003)*. The physical mechanism has been identified with the help of an energy based receptivity equation

obtained from Navier-Stokes equations without making any approximation. An example of this route of bypass transition on the attachment line, along the leading edge of an infinite swept wing, has been shown via convecting aperiodic vortices in the freestream as sub-critical instability *(Sengupta and Dipankar, 2005)*.

The classical or the bypass route of transition has been explained above for canonical flows only, while it is known that adverse pressure gradient has strong destabilizing effects on flow transition. As NLF aerofoils for general aviation purposes are of large thickness, the aft portion of the aerofoil experiences very severe varying pressure gradients, on both the top and the bottom surfaces for different angles of attack. Existence of such varying adverse pressure gradient is capable of amplifying very small background disturbances and no systematic criterion exists which theoretically correlates background disturbances with transition to turbulence for either the classical or the bypass route. In this context, it is worthwhile to investigate the process of transition over an aerofoil by direct numerical simulation of Navier-Stokes equation.

Here, we have studied flow past a NLF SHM-1 aerofoil *(Fujino et al., 2003)* which has been designed to delay flow transition at a cruise Reynolds number of *10.3* million. This is usually done by contouring the section, so that the pressure gradient delays flow transition on the suction surface, as far as possible. However, when such an aerofoil is employed for general aviation purpose, the flow eventually suffers transition in the rear half of the section due to the prevalent adverse pressure gradient which accelerates the growth rate of the trace amount of background disturbances. In a computational framework, the background disturbances can arise from various sources of numerical errors. In nature, disturbances are omnipresent and their role in destabilizing fluid flow is a pacing item of research in fluid dynamics. These disturbances can arise from surface perturbations, free-stream noise, surface vibrations etc. We emphasize that even when explicit excitation is not employed in numerical computations, due to hypersensitivity of the flow field to background disturbances at higher Reynolds numbers, transition is observed. In an ideal scenario, one would like to remove all sources of numerical errors which contribute to flow transition and then apply explicit excitations which mimic the physical background disturbances. This is possible for Blasius boundary

layer and results are reported in *(Fasel and Konzelmann, 1990; Sengupta and Bhaumik, 2011; Sengupta et al., 2009a)*. It is therefore imperative to understand the various sources of numerical errors and the way these can be eliminated or reduced. It is also equally important to choose an appropriate formulation and its accurate discretization.

The sources of errors while discretizing are (i) aliasing error in computing product terms, as explained in *(Sengupta, 2004; Sengupta et al., 2009b)*; (ii) spurious dispersive waves (whose extreme form is known as *q*-waves), as described in *(Poinsot and Veynante, 2005; Sengupta et al., 2012a; Vichnevetsky, 1982)* and due to stability, phase and dispersion error, as explained in *(Sengupta et al., 2007)*.

This paper is formatted in the following manner. In the next section, we provide the governing equation for 2D DNS performed here and its formulation. In section 3, we describe an improved orthogonal grid generation method which helps in significantly reducing numerical error. Numerical methods and analyses of these are provided in section 4. Detailed results of DNS past the SHM-1 airfoil are provided in section 5. The paper closes with a summary and conclusions.

Governing Equations and Formulation

We have obtained numerical solution of Navier-Stokes equation using stream function (ψ) - vorticity (ω) formulation. This formulation ensures solenoidality of velocity and vorticity field simultaneously and found to be more accurate, as compared to other formulations *(Sengupta, 2004)*. Also, we employ an orthogonal grid for the studied incompressible flow which allows explicit use of orthogonal formulation resulting in fewer numerical computations per time step and thereby reducing numerical errors by discretizing fewer terms with efficient discretization following the physical nature of the flow. This latter aspect is best demonstrated by the isotropic treatment of the diffusion operators in orthogonal formulation, as compared to non-orthogonal formulations. The governing Navier-Stokes equation is decoupled into kinematics and kinetics of the flow in (ψ, ω)-formulation and expressed in an orthogonal grid by the following equations

$$\frac{\partial}{\partial \xi}\left[\frac{h_{22}}{h_{11}}\frac{\partial \psi}{\partial \xi}\right] + \frac{\partial}{\partial \eta}\left[\frac{h_{11}}{h_{22}}\frac{\partial \psi}{\partial \eta}\right] = -h_{11}h_{22}\omega \qquad ....(1)$$

$$h_{11}h_{22}\frac{\partial \omega}{\partial t} + h_{22}u\frac{\partial \omega}{\partial \xi} + h_{11}v\frac{\partial \omega}{\partial \eta} =$$

$$\frac{1}{Re}\left[\frac{\partial}{\partial \xi}\left(\frac{h_{22}}{h_{11}}\frac{\partial \omega}{\partial \xi} \right) + \frac{\partial}{\partial \eta}\left(\frac{h_{11}}{h_{22}}\frac{\partial \omega}{\partial \eta} \right) \right] \quad ....(2)$$

where h_{11} and h_{22} are the scale factors used in mapping physical (x, y)-plane to a computational (ξ, η)-plane *(Sengupta, 2004)*, where ξ co-ordinate is in azimuthal direction and η is normal to it. For orthogonal mapping *(Nair and Sengupta, 1998; Sengupta et al., 2007)*, one can define the scale factors by, $h_{11} = \sqrt{x_\xi^2 + y_\xi^2}$ and $h_{22} = \sqrt{x_\eta^2 + y_\eta^2}$.

The leading and trailing edge portions of the aerofoil have a sharp slope variation and to simulate the flow correctly distribution of points on the input aerofoil geometry has to be performed judiciously by clustering more number of points in those regions. In order to resolve the boundary layer formed over the aerofoil, we have clustered the points in the η direction using a tangent hyperbolic distribution given later.

Following initial and boundary conditions are used in solving the governing equations. On the aerofoil surface, following no-slip conditions are used

$$\psi = \text{constant}, \qquad \frac{\partial \psi}{\partial \eta} = 0 \quad ....(3)$$

These conditions also help fix the wall vorticity, which is required as the boundary condition for the vorticity transport equation, Eq. (2). In O-grid topology, one introduces a cut starting from the leading edge of the aerofoil to the outer boundary. Periodic boundary conditions apply at the cut, which are introduced to make the computational domain simply-connected. For the stream function equation, Eq. (1), at the outer boundary, Sommerfeld boundary condition is used on the η-component of the velocity field. Resultant value of streamfunction is used to calculate the vorticity value at the outer boundary.

From the stream function equation the wall vorticity is calculated as

$$\omega \big|_{body} = \frac{-1}{h_{22}^2}\frac{\partial^2 \psi}{\partial \eta^2}\bigg]_{body} \quad ....(4)$$

An Improved Orthogonal Grid Generation Method

For an orthogonal mapping from physical to transformed plane, the included angle between the $\xi =$ constant and $\eta =$ constant lines in the physical plane is constrained by

$$x_\xi x_\eta + y_\xi y_\eta = 0 ....(5)$$

where the subscripts indicate partial derivative with respect to these. One can introduce a distortion function f given by

$$f = \frac{h_{22}}{h_{11}} ....(6)$$

Using Eq. (5) in Eq. (6), one gets the following two relations

$$y_\eta = -fx_\xi ....(7)$$

$$x_\eta = fy_\xi ....(8)$$

These are the well-known Beltrami equations for general orthogonal mapping *(Duraiswami and Prosperetti, 1992; Nair and Sengupta, 1998; Ryskin and Leal, 1983; Sengupta, 2004)* and these are nothing but the generalization of Cauchy-Riemann relations. The authors in *(Dipankar and Sengupta, 2006; Nair and Sengupta, 1998)* have used hyperbolic grid generation method to maintain orthogonality in a stricter sense for generated grids. This has been achieved by using Eq. (5) as one of the governing equations. In *(Steger and Chaussee, 1980)*, prescription of the cell volume given by $h_{11}h_{22}$ has been used as the second governing equation for outward marching of the equations from the boundary. In *(Nair and Sengupta, 1998)*, one of the Beltrami equations, Eqs. (7) and (8), has been used along with the orthogonality condition given by Eq. (5).

In the present work, an improved procedure for grid generation around a SHM-1 aerofoil is described step-by-step. The SHM-1 aerofoil has a camber line which results in concave surface near the trailing edge on the bottom surface, as shown in the top frame of Fig. 1(a).

In this figure, aerofoil is shown with a box A-B-C-D marking the concave part of the trailing edge. If the procedure given in *(Nair and Sengupta, 1998)* is followed up to a short distance near the aerofoil surface, then the grid-lines in the region A-B-C-D are as shown in the bottom frame of Fig. 1(a). However, if this process is continued further, then the grid-lines will eventually intersect, as indicated by the converging arrowheads in the figure. We note that even when the grid-lines move towards each other without intersection, the metric variation causes numerical difficulties associated with solution of

Navier-Stokes equation. Thus, it is imperative that grid-lines should emerge smoothly from the surface without the possibility of intersection.
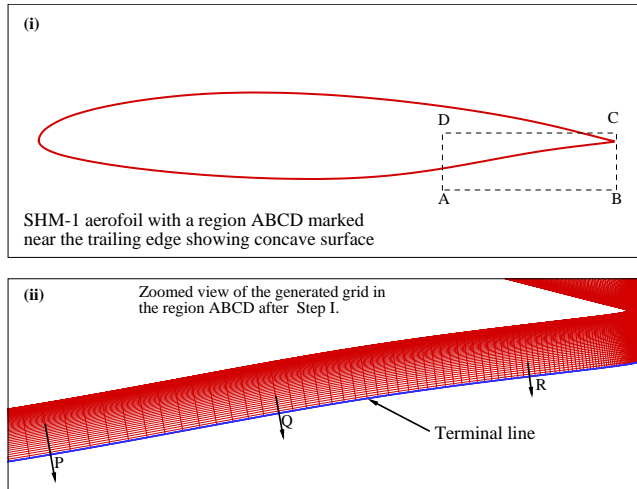

FIG. 1(a) SCHEMATIC OF SHM-1 AEROFOIL IS SHOWN IN THE TOP FRAME (I) WITH THE MARKED REGION ABCD HIGHLIGHTING CONCAVE PORTION OF THE AEROFOIL. BOTTOM FRAME (II) SHOWS ZOOMED VIEW OF THE GENERATED ORTHOGONAL GRID USING THE PROCEDURE GIVEN IN *(NAIR AND SENGUPTA, 1998)*. NOTE THE ARROWS ARE POINTED TOWARDS EACH OTHER; INDICATE PROBLEM OF GRID INTERSECTION IF THE GRID IS GENERATED CONTINUOUSLY FOLLOWING THE METHOD IN *(NAIR AND SENGUPTA, 1998)*.

The problem is acute due to the presence of concave region on the basic geometry or in the generated grid-lines subsequently. Grid intersection problem associated with concave surface can be avoided as explained below.

(I) Create an orthogonal grid around a SHM-1 aerofoil for a limited region close to the surface as shown in bottom frame of Fig. 1(a) following the procedure in *(Nair and Sengupta, 1998)*.

This is reported here as Step I and the generated grid consists of *597* points in the azimuthal direction and *80* points in the η direction. The grid is generated by taking identical spacing on η = constant line, up to *0.025c* distance from the surface of the aerofoil, where c is the chord of the aerofoil. The gap between successive η = constant lines is stretched in the η - direction following the distribution given by

$$h_{22} = H\left[1 - \frac{\tanh\left[\beta(1-\eta)\right]}{\tanh[\beta]}\right] \qquad ....(9)$$

where β represents the clustering parameter. The grid spacing in η-direction is represented by grid scale parameter h_{22} and H is the non-dimensional (in terms of chord of the aerofoil) distance of the outer boundary.

(II) To circumvent problems of grid intersection, concavity is gradually removed from successive η = constant lines as one marches outward from the aerofoil. The concave region is identified by plotting $\partial^2 y/\partial x^2$ parameter as a function of points on the terminal line of the grid region. The concave part of the terminal line is shown clearly by the positive values on the top surface and negative values below the bottom surface. For the generated grids' terminal line, this is shown dotted in Fig. 1(b).

If h_{22} in the concave region is increased, then the concavity will be reduced progressively as we move away from aerofoil surface, as shown by the circular symbols in Fig. 1(b). We have limited the absolute magnitude of the curvature on top and bottom surfaces to a threshold value of *0.25* to ensure removal of concavity. Threshold value is reached by changing h_{22} by a small magnitude in an iterative fashion, as rapid change causes grid intersection. Although, the problem associated with grid line intersection due to
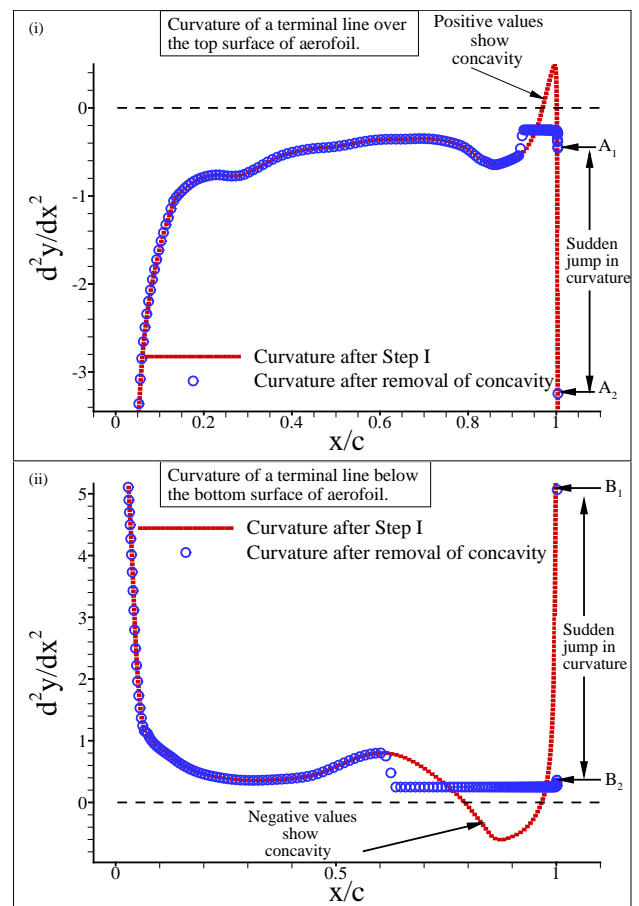

FIG. 1(b) VARIATIONS OF CURVATURE ON THE TERMINAL LINE OF THE GENERATED GRID ARE SHOWN: (I) OVER THE TOP SURFACE OF THE AEROFOIL AND (II) BELOW THE BOTTOM SURFACE OF THE AEROFOIL. NOTE THAT THE CONCAVITY FROM THE TERMINAL LINE OF THE GENERATED GRID HAS BEEN REMOVED COMPLETELY.

concavity is removed, one ends up with curvature discontinuities, as marked by points A_1, A_2 and B_1, B_2 in Fig. 1(b). Such discontinuities cause discontinuous variation of grid metrics. This is avoided by the following.

Next, we do not prescribe a constant threshold limit at all points on the terminal line, instead the threshold value varies with ξ. These threshold limits are obtained by using weighted average procedure at the ith node by

$$\frac{\partial^2 y}{\partial x^2}|_i = 0.50\left(\frac{\partial^2 y}{\partial x^2}|_{i+1} + \frac{\partial^2 y}{\partial x^2}|_{i-1}\right)$$

The h_{22} is again adjusted in an iterative manner so that points on the terminal line achieve the prescribed smooth curvature. This procedure removes the discontinuities in the curvature, as shown in Fig. 1(c). As noted earlier, curvature was discontinuous as marked by points A_1, A_2 and B_1, B_2. This step removes the sharp curvature variation with addition of few more points, as shown in Fig. 1(c).
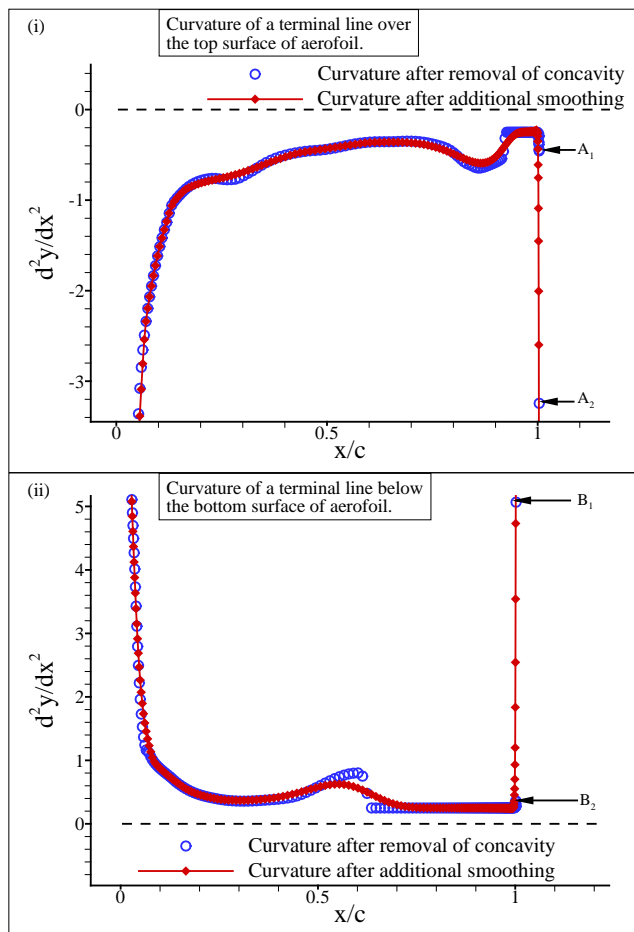

FIG. 1 (c) VARIATION OF CURVATURE ON THE TERMINAL LINE OF THE GENERATED GRID IS SHOWN: (I) OVER THE TOP SURFACE OF THE AEROFOIL AND (II) BELOW THE BOTTOM SURFACE OF THE AEROFOIL AT THE END OF STEP II

Grid generated at the end of this step is shown in the top frame of Fig. 1(d). Marked arrows clearly show that the grid concavity has been removed, as also seen in the bottom frame of Fig. 1(d). Here, we have shown the trailing edge of SHM-1 aerofoil along with the terminal lines of the generated grid after Steps I and II. Concavity is thus, removed completely by the procedure of filling the gap in Step II.

(III) In this step, we further generate grid lines by marching away from the terminal line of Step II up to desired outer boundary. This step completes the grid generation process.
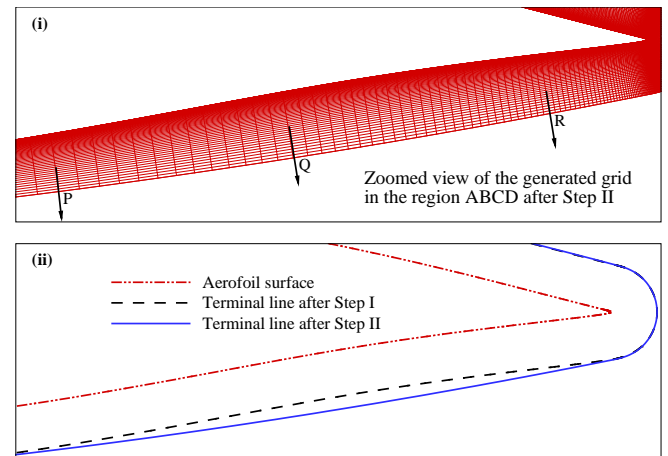

FIG. 1(d) ZOOMED VIEW OF THE GENERATED ORTHOGONAL GRID AT THE END OF STEP II IS SHOWN IN THE TOP FRAME (I). NOTE THE CONCAVITY PRESENT IN THE INITIALLY GENERATED GRID HAS BEEN REMOVED AT THE END OF STEP II, AS SHOWN IN THE BOTTOM FRAME (II)
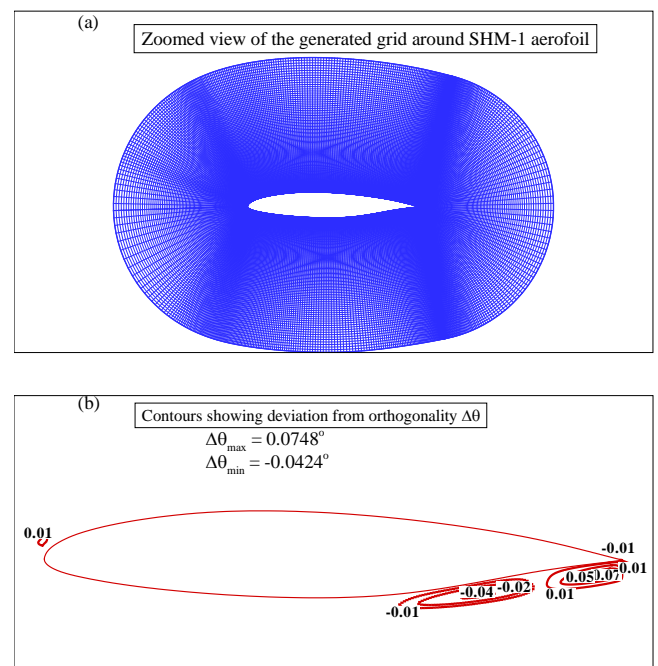

FIG. 2(a) ZOOMED VIEW OF THE GENERATED GRID AFTER STEP III IS SHOWN; (b) CONTOURS OF DEVIATION FROM ORTHOGONALITY ARE SHOWN FOR THE GENERATED GRID

Here we have constructed a final grid of *597 X 397* points and outer boundary located at a distance of 14*c* from the aerofoil surface. A zoomed view of the generated grid is shown in Fig. 2(a). Deviation of grid lines from orthogonality is shown in the contour plot of Fig. 2(b). The maximum deviation from orthogonality ($\Delta\theta_{max}$) is *0.0748°* and the minimum deviation ($\Delta\theta_{min}$) is *-0.0424°*. This is one order less deviation as compared to *0.524°* reported for the case of NACA 0015 aerofoil in *(Nair and Sengupta, 1998)*. This establishes the present grid generating algorithm that has a capability to generate grid around concave shaped bodies with negligible deviation from orthogonality.

Analyses of Numerical Methods

Before obtaining numerical solutions, we show numerical properties of the used high accuracy space-time discretization scheme (*SOUCS3-OCRK3*), as explained with properties in Fig. 3. Details of the space and time discretization methods can be seen in *(Sengupta et al., 2011a)*. Firstly, we compare the spectral resolution of *SOUCS3* method with some conventional *spatial* discretization schemes used to obtain the first derivatives in Eq. (2).

If a variable is defined by its Laplace transform as $u(x,t) = \int U(k,t)\, e^{ikx}\, dk$, then its exact spatial derivative is

$$\left(\frac{\partial u}{\partial x}\right)_{ex} = \int ik\ U(k,t)e^{ikx}dk$$

When this derivative is obtained numerically, it is written equivalently as $\left(\dfrac{\partial u}{\partial x}\right)_{num} = \int ik_{eq}\ U(k,t)e^{ikx}dk$

In Fig. 3(a), spatial resolution for the first derivative given by real part of k_{eq}/k for central second order scheme CD_2; for fourth order central discretization scheme CD_4, along with the compact scheme *SOUCS3* *(Sengupta et al., 2011a)*, is compared as a function of non-dimensional wavenumber (*kh*), up to the Nyquist limit, with *h* representing the uniform grid spacing in the transformed plane. Ideally the ordinate should be equal to one across the complete *kh* range. However, phase mismatch amounts to filtering the unknown in obtaining the derivative numerically. Note that CD_2 method produces highest filtering at all wavenumbers, while *SOUCS3* scheme has near-spectral accuracy over a larger range. From Fig. 3(a), *SOUCS3* is seen to resolve first derivative over a range by order of magnitude, as compared to the CD_2 scheme in each

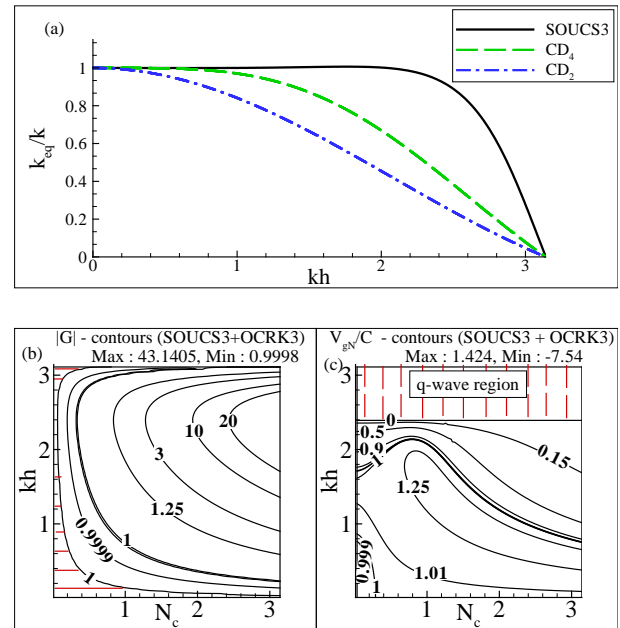direction, leading to significantly enhanced ability of DNS by such compact schemes.

FIG. 3(a) COMPARISON OF SCALE RESOLUTION BETWEEN SECOND ORDER, FOURTH ORDER CENTRAL DIFFERENCE SCHEME AND THE COMPACT SCHEME *SOUCS3* USED HERE; (b) |*G*| AND (c) V_{gN}/C CONTOURS FOR THE SOLUTION OF 1D CONVECTION EQUATION USING THE *SOUCS3-OCRK3* SCHEME. NOTE THE PRESENCE OF *q*-WAVE REGION AT HIGHER WAVENUMBER RANGE IN (c)

However, one must also ensure that the adopted method correctly propagates energy and phase of created disturbance field maintaining perfect neutral stability, as emphasized in *(Sengupta et al., 2007)*, with respect to the analysis of space-time discretization schemes for the linear convection equation

$$\frac{\partial u}{\partial t} + C\frac{\partial u}{\partial x} = 0 \cdots\cdots\cdots\cdots\cdots\cdots\cdots (10)$$

Equation (10) convects the initial solution to the right at the group velocity, which is equal to the phase speed *C*, at all time due to non-dispersive nature. Following the analysis of *(Sengupta et al., 2007)*, we show the numerical amplification factor |*G*|-contours and numerical group velocity V_{gN}/C-contours for the solution of Eq. (10) using *SOUCS3* and *OCRK3* schemes in Figs. 3(b) and 3(c).

The numerical stability is defined by the amplification factor $G(k, \Delta t) = U(k, t+\Delta t)/U(k, t)$ which is a complex quantity. Numerical dispersion relation is obtained in terms of $\tan\beta = -G_{imag}/G_{real}$ and numerical group velocity has been obtained in *(Sengupta et al., 2007; Sengupta et al., 2011a)* as,

$$\frac{V_{gN}}{C} = \frac{1}{N_c}\frac{\partial \beta}{\partial (kh)}$$

with the Courant-Friedrich Lewy (CFL) number defined by $N_c = C \, \Delta t / \Delta x$.

In Fig. 3(b), $|G|$-contours are shown for SOUCS3-OCRK3 scheme in (N_c, kh)-plane for the solution of Eq. (10). The $|G|$-contours have the desirable neutrally stable property across the fully resolved length scales, only for a narrow range of small N_c values, shown by the hatched region in the figure. The other important dispersion property of the numerical method relates to preserving the actual physical dispersion relation is shown in the (N_c, kh)-plane, in Fig. 3(c). DRP property is retained effectively for a significant kh and N_c range. Figure 3(c) also shows that choice of kh should be restricted below $kh = 2.4$, as the solution components above this non-dimensional wavenumber travel in the opposite to the physical direction, due to negative values of numerical group velocities, shown by vertical hatched lines in Fig. 3(c). This is the region, which will be responsible for spawning q-waves. Extreme form of spurious dispersion associated with q-waves leads to unphysical propagation which may lead to numerical instabilities.

Use of conventional central one-dimensional (1D) filters, as proposed in *(Gaitonde et al., 1999)* cannot rectify the problem of q-waves for any value of N_c as shown in Fig. 3(c). So a new fifth order upwind filter has been introduced in *(Sengupta et al., 2009)*, which has the additional capability of modifying numerical dispersion relation so that q-wave region is removed for a small range of N_c. Effectiveness of a filter while filtering different wavenumber components is shown by its transfer function (*Bhumkar and Sengupta, 2011; Sengupta et al., 2009*) and in Figs. 4(a) and 4(b), we have shown real and imaginary parts of the transfer functions for the fifth order upwinded filter corresponding to a central node. In these plots, we have chosen value of filtering coefficient $\alpha_1 = 0.45$ and upwind parameter $\eta_1 = 0.001$. Note that transfer function of a filter has both real and imaginary parts. The real part shown in Fig. 4(a), indicates the amount of attenuation imposed by the filter at different scales. Simultaneous presence of real and imaginary parts for the transfer function of upwind filter ensures alteration of the dispersion property. Combined action of both real and imaginary parts of the transfer function modifies the numerical amplification factor as shown in Fig. 4(c) for the solution of Eq. (10), by SOUCS3-OCRK3 schemes.

One observes attenuation of high wavenumber components which are responsible for numerical

instabilities. Corresponding numerical group velocity contours are shown in Fig. 4(d) with the unique feature of complete removal of q-waves for a small range of N_c values up to $N_c = N_{cr}$ as marked in Fig. 4(d).
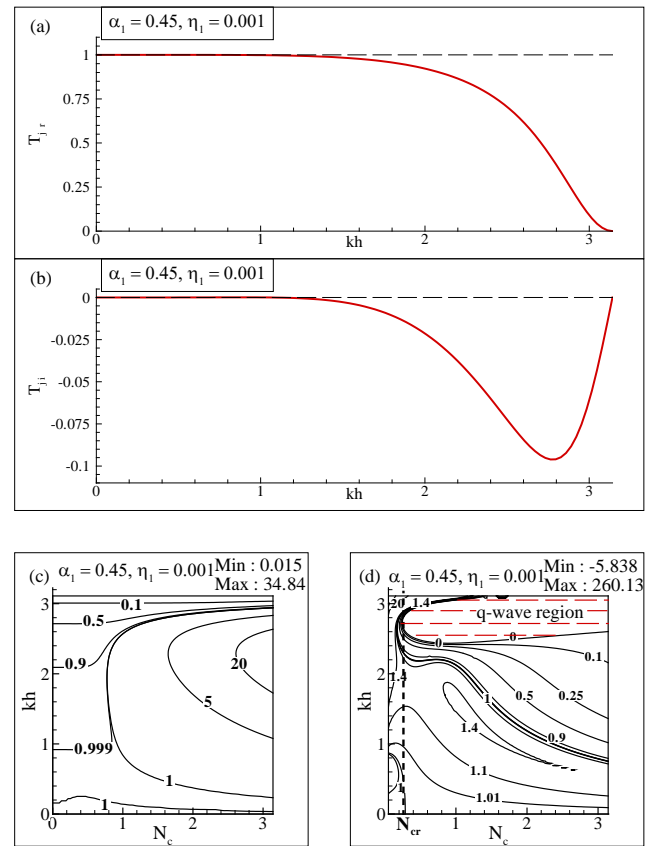

FIG. 4 VARIATIONS OF (a) REAL PART AND (b) IMAGINARY PART OF THE TRANSFER FUNCTIONS OF THE FIFTH ORDER UPWIND FILTER (*SENGUPTA ET AL., 2009*) FOR FILTER COEFFICIENT $\alpha_1 = 0.45$ AND $\eta_1 = 0.001$ ARE SHOWN ALONG WITH MODIFICATIONS IN (c) $|G|$ AND (d) V_{gN}/C CONTOURS FOR THE CASE OF FIG. 3. NOTE THE q-WAVE REGION HAS BEEN REMOVED OVER A SMALL RANGE OF N_{cr} IN (d)

Although, problems associated with q-waves are successfully handled by using 1D upwind filter *(Sengupta et al., 2009)*, aliasing error is also another significant source of error in the computations obtained by high accuracy numerical methods. To control the aliasing error effectively and at the same time to limit the extra computational cost of filtering, a multi-dimensional adaptive filter has been introduced in *(Bhumkar and Sengupta, 2011)*, where a 2D filter is used in a limited region wherever needed. General form of 2D filters *(Bhumkar and Sengupta, 2011)* is given by

$$\hat{u}_{i,j} + \alpha_{2f} \left(\hat{u}_{i-1,j} + \hat{u}_{i+1,j} + \hat{u}_{i,j-1} + \hat{u}_{i,j+1} \right) =$$
$$\sum_{n=0}^{M} \frac{a_n}{2} \left(u_{i \pm n, j} + u_{i, j \pm n} \right) \quad ....(11)$$

where M is the order of the filter and is equal to one for a 2D second order filter. The coefficients $a_n's$ are related to user defined filtering coefficient α_{2f} and their role is to smooth selectively the higher wavenumber fluctuations. In the above, increase of M by one, increases the order of the filter by two. Equation (11) is used for points inside the computational domain and solved iteratively using *Bi-CGSTAB* method (Vorst, 1992). As these equations are solved iteratively, significant computational efforts are needed if filtering is performed over the complete domain. It has been shown in *(Bhumkar and Sengupta, 2011)* that filtering can be performed in an adaptive manner over small patches, whenever required.
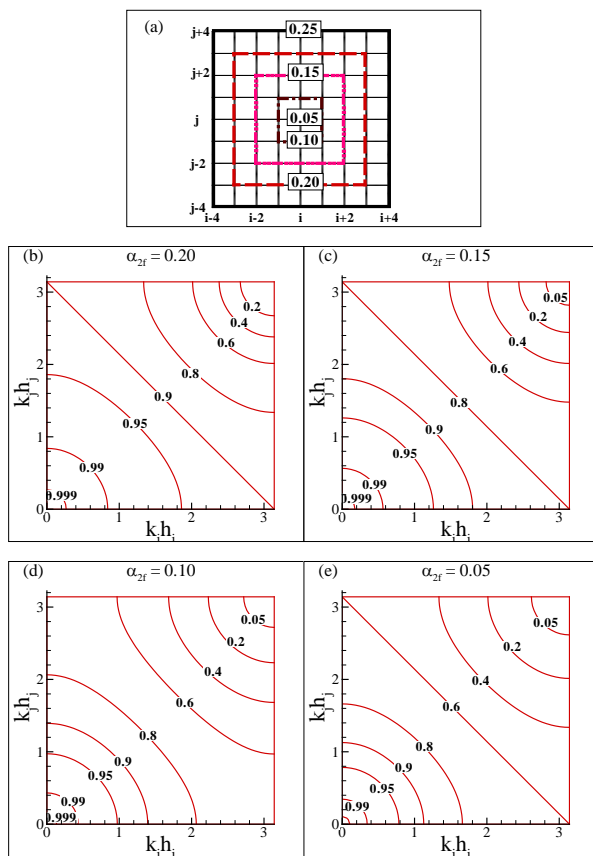

FIG. 5 (a) SCHEMATIC OF THE ADAPTIVE 2D FILTERS *(BHUMKAR AND SENGUPTA, 2011)* WITH THE FILTER SUB-DOMAIN SHOWN IN THE TRANSFORMED PLANE. FOR THE 2D FILTERS, THE TRANSFER FUNCTIONS ARE SHOWN IN FRAMES (b) TO (e) FOR DIFFERENT VALUES OF THE FILTER COEFFICIENT α_{2f}.

For this purpose, one identifies a square sub-domain in the transformed plane where filtering is performed smoothly, as shown in Fig. 5(a) by the (*9 X 9*) points filter-tent used in the adaptive filter. Variation of filter coefficient α_{2f} over the tent is also shown in this frame. Corresponding transfer function variations in ($k_i h_i$, $k_j h_j$)-plane are shown in frames 5(b) to 5(e). The region corresponding to ($k_i h_i + k_j h_j$) > π contributes to aliasing

error and the transfer functions of this multi-dimensional filter effectively attenuate the aliasing error without causing alteration of the lower wavenumbers as discussed in *(Bhumkar and Sengupta, 2011)*. Aliasing error results from the evaluation of product terms in a finite grid. Computations of nonlinear product terms or even the computations of linear terms in a transformed domain lead to aliasing error.

For example in Eqs. (1) and (2), nonlinear product terms appear when the computations are performed in a transformed plane even for linear diffusion terms. This problem accentuates at low Reynolds number in Eq. (2) for the viscous diffusion terms, as this is multiplied by *1/Re* and involves evaluating triple product terms. It is to be noted that the product evaluations involving derivatives using higher accuracy methods are more prone to aliasing error due to the inherent filtering operation of derivative by any discrete methods excepting Fourier spectrum method. However, lower accuracy methods filter more in obtaining the derivatives and hence suffer lesser aliasing.
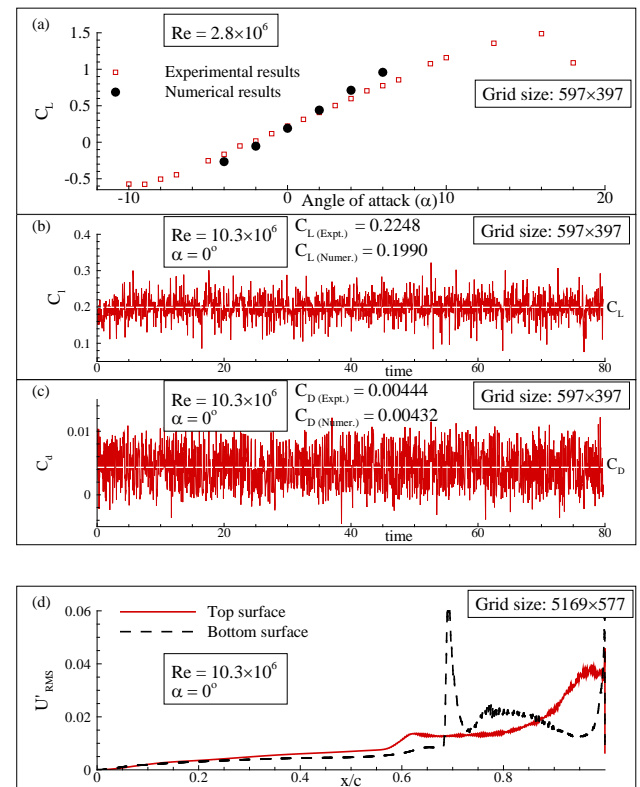

FIG. 6 (a) NUMERICALLY OBTAINED C_L WITH ANGLES OF ATTACK IS SHOWN ALONG WITH EXPERIMENTAL RESULTS OF *(FUJINO ET AL., 2003)*; VARIATION OF INSTANTANEOUS C_l AND C_d IS SHOWN IN FRAMES (b) AND (c), RESPECTIVELY; (d) VARIATION OF RMS VALUE OF THE AZIMUTHAL COMPONENT OF THE VELOCITY OVER AEROFOIL FOR *RE = 10.3 X 10⁶* ON A LINE CLOSE TO THE AEROFOIL

Results and Discussion

Next, we validate our numerical results with the experimental results provided in *(Fujino et al., 2003)*. Here, we have reported results for two Reynolds number cases, *Re = 2.8 X 10⁶* and *Re = 10.3 X 10⁶* using a (*597 X 397*) grid. In Fig. 6(a), we have compared variation of numerically obtained mean lift coefficient (*C_L*) with angle of attack for *Re = 2.8 X 10⁶* with the experimental results provided in *(Fujino et al., 2003)*. Comparison shows a good match between the numerical and experimental values. The present calculations are strictly two-dimensional for *Re = 2.8 X 10⁶* without any explicit forcing for the case shown in Fig. 6(a), while the experimental results involve three-dimensionality and background tunnel noise.

Time variations of lift and drag coefficient for *Re = 10.3 X 10⁶* and zero angle of attack are shown in frames (b) and (c), respectively. Time averaged values of lift and drag coefficients are shown with the horizontal dashed lines in these frames. Results show a good match between the experimental and numerically obtained values. Although, computations reported with a (*597 X 397*) grid show a good comparison with the experimental results, next we report the numerical results obtained by using a finer (*5169 X 577*) grid specifically for a careful study of flow transition over a NLF aerofoil. Variation of RMS value of azimuthal component of disturbance velocity over top and bottom surfaces is shown in Fig. 6(d) at a distance of *0.000056c* from the aerofoil surface. Variation of RMS component over the aerofoil surface shows that after *60%* of chord there is sharp rise in fluctuations on the top surface indicating flow transition similar to the experimental results shown in *(Fujino et al., 2003)*. On the bottom surface, one notes even a sharper variation of the RMS component of azimuthal velocity at *x = 0.70c*. Correct prediction of transition location highlights importance of highly space-time accurate numerical solutions obtained here.

We have computed flow past SHM-1 aerofoil for *Re = 10.3 X 10⁶* at zero angle of attack and Fig. 7(a) shows streamfunction contours at *t = 4.50* for this flow. Top frame shows the flow field around the complete aerofoil, while in the bottom frame; flow field near the trailing edge of the aerofoil is shown at the same instant. Flow near the leading edge of the aerofoil experiences acceleration due to the favourable

pressure gradient. As flow moves towards trailing edge, it experiences progressive adverse pressure gradient. Due to varying adverse pressure gradient, small separation bubbles are formed on the aerofoil surface near trailing edge which moves downstream along with the flow. These separation bubbles are observed in the zoomed view of a trailing edge as shown in the bottom frame of Fig. 7(a). As these bubbles move towards the trailing edge, these further excite the flow field. As shown earlier in Fig. 6(d), flow transition on top surface starts after *0.60c*, these separation bubbles also first appear around the same location. In Fig. 7(b), variations of displacement thickness *δ** on top and bottom surfaces of SHM-1 aerofoil are shown in frame (i) up to *60%* of chord of SHM-1 aerofoil at *t = 4.50*. Additionally, variation of a steady flow separation parameter used in Falkner-Skan analysis, *m= (x/U_e)($\partial U_e / \partial x$)*, is shown for the top and bottom surfaces of SHM-1 aerofoil in frame (ii) *at t = 4.50*.
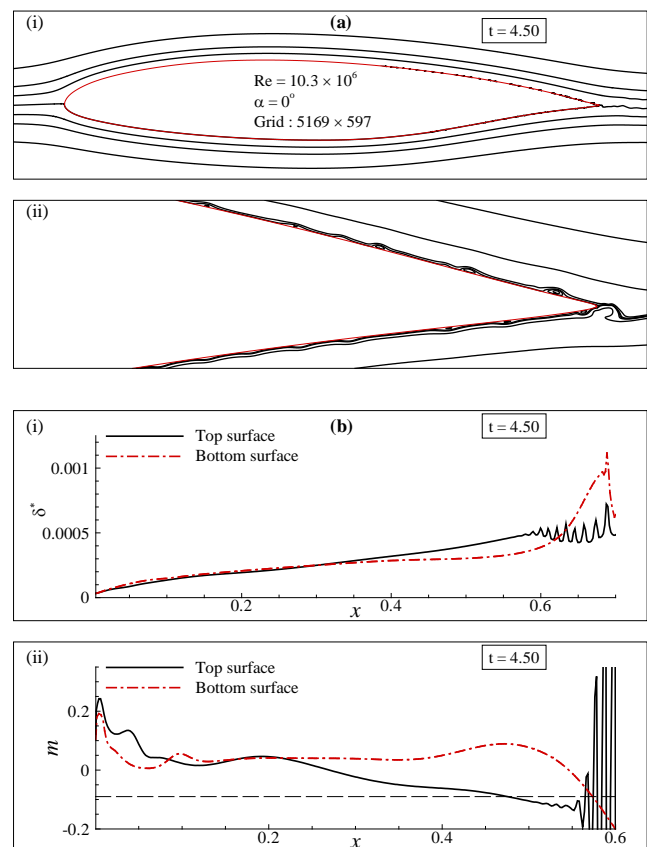

FIG. 7 (a) STREAM FUNCTION CONTOURS OVER THE COMPLETE AEROFOIL AS WELL AS NEAR THE TRAILING EDGE ARE SHOWN FOR THE INDICATED PARAMETERS; (b) VARIATION OF THE DISPLACEMENT THICKNESS *δ** AND STEADY FLOW SEPARATION PARAMETER *m*, ON TOP AND BOTTOM SURFACES OF SHM-1 AEROFOIL IS SHOWN IN FRAMES (I) AND (II), RESPECTIVELY
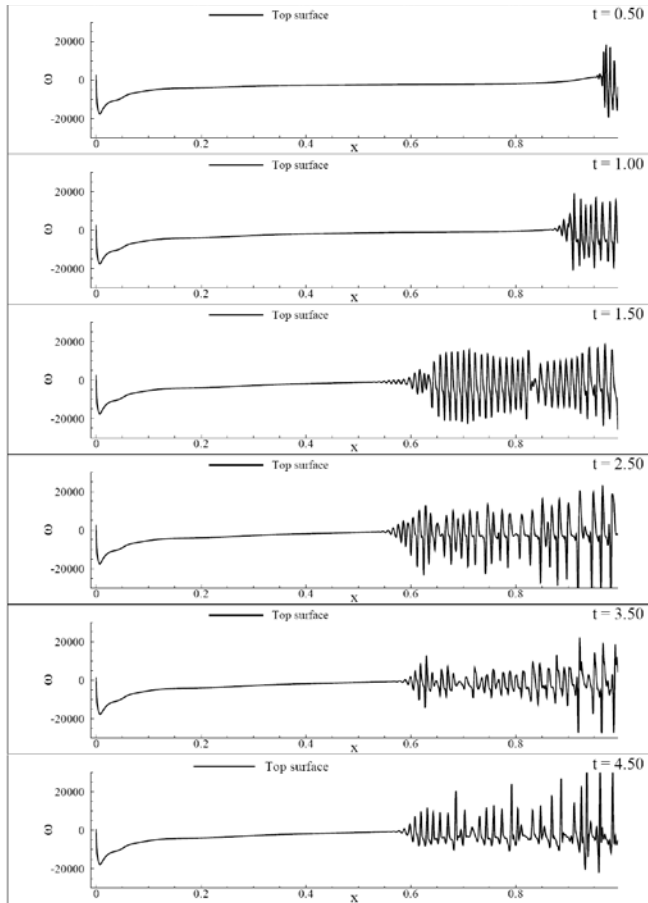
FIG. 8 (a) VARIATION OF WALL VORTICITY ON THE TOP SURFACE OF SHM-1 AEROFOIL HAS BEEN SHOWN FOR THE CASE OF *RE = 10.3* MILLION AND $\alpha = 0^O$, AT THE INDICATED TIMES

A horizontal dashed line corresponding to steady separation flow criterion (*m*= -0.09) is marked for comparison purpose. Figure shows that on the top surface near the leading edge, flow experiences higher favourable pressure gradient, as compared to the bottom surface. Pressure gradient parameter (*m*) smoothly decreases on the top surface after the initial peak near the leading edge. However, on the bottom surface, pressure gradient parameter remains favourable to a larger distance from the leading edge of the aerofoil and then it has a sharp variation aft of the mid-chord location.

Variation of surface vorticity on the top and the bottom surfaces at different time instants are shown in Figs. 8(a) and 8(b), respectively. Due to acceleration of flow near the leading edge on the top surface, one notices sharp vorticity variation near the leading edge. Formation of wavy disturbances on the top surface starts approximately from *x = 0.55c* onwards, while on the bottom surface, these disturbances start appearing from *x = 0.70c* onwards. Time variation of surface vorticity shows that disturbances on the bottom

surface have similar range of vorticity variation as compared to the disturbances on the top surface. Flow field in the second half part of the aerofoil shows strong unsteady behaviour, as compared to first half, even when no explicit excitation is applied.
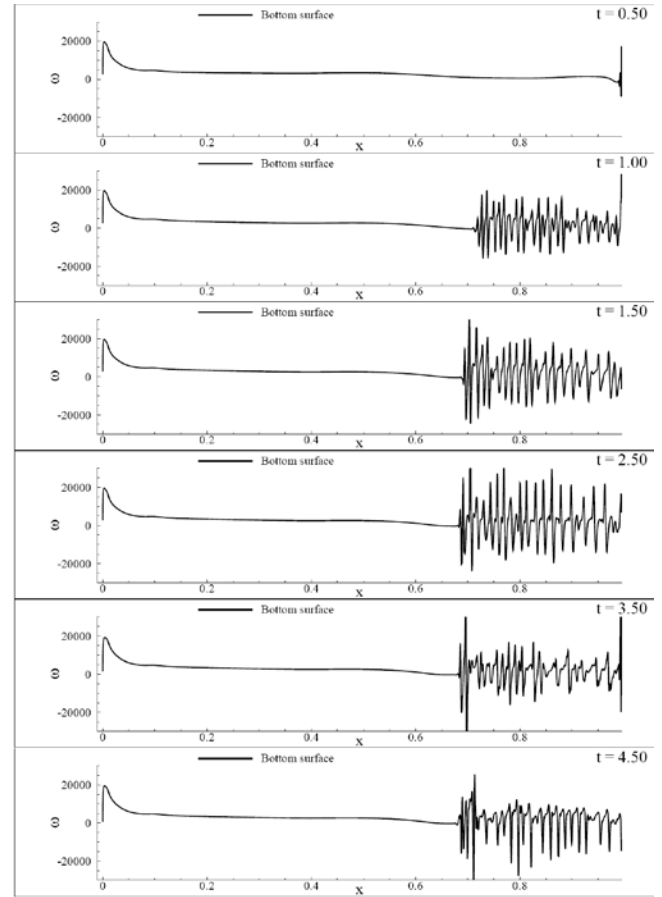

FIG. 8 (b) VARIATION OF WALL VORTICITY ON THE BOTTOM SURFACE OF SHM-1 AEROFOIL HAS BEEN SHOWN FOR THE CASE OF *RE = 10.3* MILLION AND $\alpha = 0^O$, AT THE INDICATED TIMES

Formation and propagation of separation bubbles on the top surface is shown in Fig. 9(a). Variation of the azimuthal component of the velocity (*u*) at a distance of *1.242 X 10⁻⁶c* from the top surface of the SHM-1 aerofoil is traced in this figure, with time. This height corresponds to the second azimuthal line (*η* = constant line) from the aerofoil surface. At *t = 0.40*, small wavy disturbances appear originating from the trailing edge. These disturbances move upstream with time as noted in the subsequent frames. Presence of adverse pressure gradient near the trailing edge magnifies these disturbances, which propagate further upstream as shown in this figure. The calculations are performed on a finer grid with (*5169 X 577*) points, to resolve the length scales correctly and avoid aliasing error. Additionally, we have used upwind filter (*Sengupta et al., 2009*) to prevent any *q*-waves contaminating the

numerical solution. So the upstream propagation of the disturbances suggest physical bypass transition phenomenon *(Sengupta, 2012)* and not due to *q*-waves. Figure 9(a) shows how additional wave-packets are introduced upstream of this propagating main disturbance, marked as T_v in the frames at *t=1.25* and later. This induced wave packet (T_v) grows quite rapidly, as noted from the frames from *t=1.25* to *t=1.31*, while convecting downstream. As time progresses, this sequence of upstream migration of disturbance fronts fill up the top surface, up to about *x = 0.55c*, at around *t =1.50*. Thereafter, disturbances formed on the top surface stop upstream propagation and continue to convect downstream, as shown till *t =4.50*.
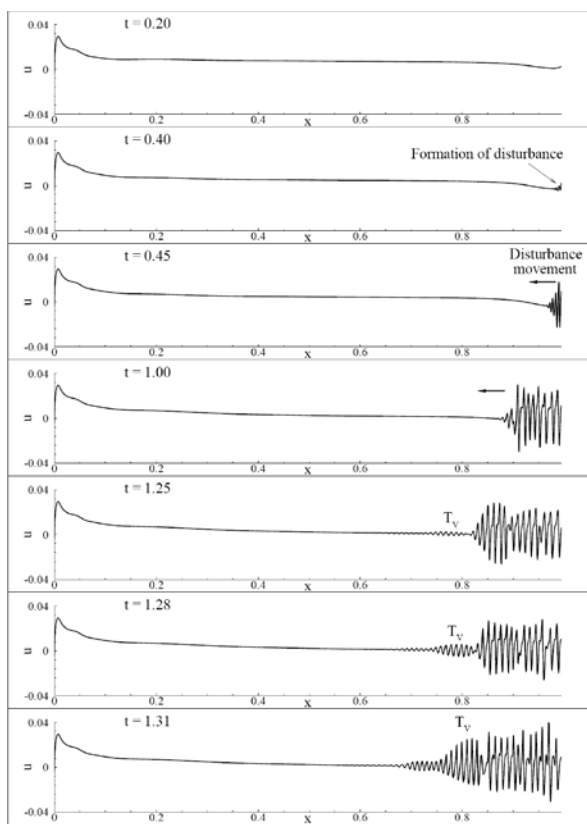

FIG. 9 (a) VARIATION OF THE AZIMUTHAL COMPONENT OF THE VELOCITY (*U*) AT A DISTANCE OF *1.242 X 10⁻⁶ c* FROM THE TOP SURFACE OF SHM-1 AEROFOIL HAS BEEN SHOWN FOR THE CASE OF *RE = 10.3 X 10⁶* AND *α = 0ᴼ*, AT THE INDICATED TIMES. (CONT)

Similar formation and propagation of disturbances on the bottom surface is shown in Fig. 9(b). In this figure, once again the variation of azimuthal component of the velocity (*u*) is shown at a distance of *1.242 X 10⁻⁶c* from the bottom surface. Similar to top surface, wavy disturbances originate from the trailing edge and can be observed as early as at *t = 0.50*. By   *t = 0.67*, an induced small disturbance packet is noted close to x = *0.8c*, which is marked as B_v. Its rapid growth is traced

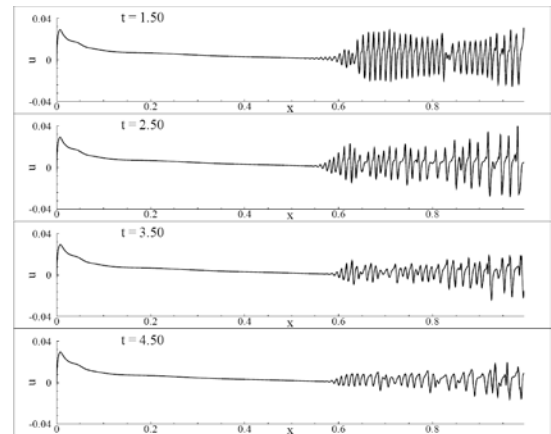in the subsequent time frames and one can note the nonlinear distortion by *t = 0.71*.

FIG. 9 (a) VARIATION OF THE AZIMUTHAL COMPONENT OF THE VELOCITY (*U*) AT A DISTANCE OF *1.242 X 10⁻⁶ c* FROM THE TOP SURFACE OF SHM-1 AEROFOIL HAS BEEN SHOWN FOR THE CASE OF *RE = 10.3 X 10⁶* AND *α = 0ᴼ*, AT THE INDICATED TIMES

The trailing edge position near *x = 0.8c* of the aerofoil has large concavity imposing strong adverse pressure gradient, which results in such drastic amplification of disturbances. Due to nonlinear action, unsteady separation bubbles are formed in this part of the aerofoil, resulting in increased drag. As compared to the top surface, here the upstream location of the disturbance is restricted up to *x = 0.70c*, as noted in the bottom frames of Fig. 9(b).

Summary and Conclusions

Here, we report the DNS results of transitional flow over a NLF aerofoil (SHM-1) for the cruise Reynolds number of *10.3* million. To perform such DNS, one must first identify the need for high accuracy computing to capture the physical processes of transition to turbulence. The major computational elements essential for DNS have been identified here first by reducing various sources of numerical errors. In the present work, we have systematically removed these by use of appropriate grid, numerical method and post-processing tools.

An algorithm to generate a truly orthogonal grid for thick and cambered aerofoil is developed and explained with the help of Figs. 1(a) to 1(d), by removing grid shocks arising from the concave part of the aerofoil near the trailing edge. The resultant orthogonal grid for SHM-1 NLF aerofoil is shown in Fig. 2, with highest departure from orthogonality is noted for a single point as *0.0748ᵒ* in Fig. 2(b). Thus, one can solve Navier-Stokes equation in orthogonal

formulation, which reduces numerical errors as compared to non-orthogonal formulation. Efficiency of the proposed grid generation algorithm in constructing orthogonal grid around cambered aerofoils is a significant element of the present procedure.
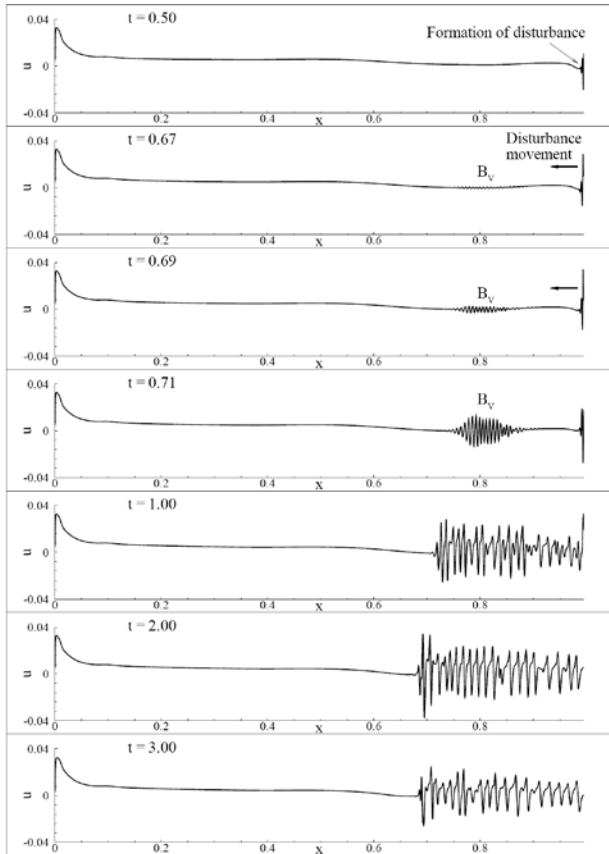

FIG. 9 (b) VARIATION OF THE AZIMUTHAL COMPONENT OF THE VELOCITY (U) AT A DISTANCE OF *1.242 X 10⁻⁶ c* FROM THE BOTTOM SURFACE OF SHM-1 AEROFOIL HAS BEEN SHOWN FOR THE CASE OF *RE = 10.3 X 10⁶* AND $\alpha = 0^O$, AT THE INDICATED TIMES

Above mentioned orthogonal grid used with orthogonal formulation is further aided by adopting high accuracy method in solving vorticity transport equation. High resolution ability of the used *SOUCS3 (Dipankar and Sengupta, 2006)* scheme in discretizing convection terms is demonstrated by comparing the equivalent numerical wavenumber in the spectral plane with conventional second and fourth order discretization methods in Fig. 3(a). The compact scheme has higher resolution by almost an order of magnitude, as compared to second order discretization. This spatial discretization is used to develop a DRP scheme for time integration, as the *OCRK3* scheme in (Sengupta et al., 2011a), which is used here. These combined schemes are calibrated with respect to the model 1D convection equation and

the contours of numerical amplification factor $|G|$ and numerical group velocity V_{gN}/C, are shown in Figs. 3(b) and 3(c), respectively. Despite providing superior discretization properties, one notices a range of high wavenumber components ($kh \geq 2.40$) displaying spurious dispersion, with V_{gN}/C contours taking negative values. Such spurious upstream propagation gives rise to *q*-waves, which has been removed for a small N_c range by using a fifth order upwind filter (*Sengupta et al., 2009)*, whose transfer function and effects on numerical properties are shown in Fig. 4.

It is known that high accuracy methods also suffer from aliasing error for high Reynolds number computations. This has been controlled by using an adaptive multi-dimensional filter (Bhumkar and Sengupta, 2011), whose transfer function is shown in Fig. 5 for different filter coefficient values. Resultant method is calibrated by comparing experimental results *(Fujino et al.,* 2003*)* and numerically-obtained time-averaged lift coefficient with angle of attack, for *Re = 2.8* million in Fig. 6(a). Time histories of lift and drag coefficients in Fig. 6(b) and 6(c), show good match between computational and experimental time averages for *Re = 10.3* million. Variation of RMS component of azimuthal disturbance component of velocity is shown in Fig. 6(d), showing flow transition to occur after *0.60c* on the top surface and after *0.70c* on the bottom surface.

Numerical results have also been obtained for *Re = 10.3* million, at zero angle of attack, using a very fine grid with *5169 X 577* points, which are shown in Figs. 7 to 9. Results show that due to high adverse pressure gradient, initially disturbances originate near the trailing edge on both top and bottom surfaces and with time these propagate upstream. Upstream movement of these disturbances is restricted up to *x = 0.55c* on top surface and *x = 0.70c* on bottom surface of aerofoil. The top surface data matches with the experimental data in *(Fujino et al., 2003)*, while there are no data available for transition on the bottom surface.

Present exercise needs to be carried out with the application of realistic explicit background disturbances in wind tunnels to highlight the role of freestream turbulence in fixing the loads on aerofoil, specifically the drag coefficient. This would require not only the use of fine grids, but also proper description of free stream turbulence in the tunnel and its appropriate model.

REFERENCES

Bhumkar, Y.G., Sengupta, T.K., "Adaptive multi-dimensional filters", Computers and Fluids, vol. 49, pp.128-140, 2011.

Dipankar, A., Sengupta, T.K., "Symmetrized compact scheme for receptivity study of 2D transitional channel flow", Journal of Computational Physics, vol. 215, pp.245–273, 2006.

Drazin, P.G., Reid, W.H., *"Hydrodynamic Stability"*, Cambridge Univ. Press, Cambridge, 1981.

Duraiswami, R., Prosperetti, A., "Orthogonal mapping in two dimensions", Journal of Computational Physics, vol. 98 pp.254–268, 1992.

Eca, L., "2D orthogonal grid generation with boundary point distribution control", Journal of Computational Physics, vol. 125, pp.440–453, 1996.

Fasel, H., Konzelmann, U. "Non-parallel stability of a flat-plate boundary layer using the complete Navier-Stokes equations", Journal of Fluid Mechanics, vol. 221, pp. 311–347, 1990.

Fujino, M., Yoshizaki, Y., Kawamura, Y., "Natural-laminar flow airfoil development for a lightweight business jet", Journal of Aircraft, vol. 40(4), pp.609–615, 2003.

Gaitonde, D.V., Shang, J.S., Young, J.L., "Practical aspects of higher-order numerical schemes for wave propagation phenomena", International Journal of Numerical Methods in Engineering, vol. 45, pp.1849–1869, 1999.

Heisenberg, W., "Über Stabilität und turbulenz von Flüssigkeitsströmen", Annalen der Physik Leipzig, vol. 74, pp.577–627, 1924.

Lim, T.T., Sengupta, T.K., Chattopadhayay, M., "A visual study of vortex induced subcritical instability on a flat plate laminar boundary layer", Experiments in Fluids, vol. 37, pp.47–55, 2004.

Morkovin, M.V., "On the many faces of transition", in: Wells CS, editor. *Viscous Drag Reduction* 1-31, Plenum Press, New York, 1969.

Nair, M.T., Sengupta, T.K., "Orthogonal grid generation for Navier-Stokes computations", International Journal for Numerical Methods in Fluids, vol. 28, pp.215–224, 1998.

Poinsot, T., Veynante, D., *"Theoretical and Numerical Combustion"*, 2nd Edn., R.T. Edwards Inc., Philadelphia, 2005.

Ryskin, G., Leal, L., "Orthogonal mapping", Journal of Computational Physics, vol. 50, pp.71–100, 1983.

Schlichting, H., "Zur Entstehung der Turbulenz bei der Plattenströmung", Nachr. Ges. Wiss. Göttingen, Math. -phys. Kl. Vol. 42, pp.181–208, 1933.

Schubauer, G.B., Skramstad, H.K., "Laminar boundary layer oscillations and transition on a flat plate", NACA Report 909, 1947.

Sengupta, T.K., *"Fundamentals of Computational Fluid Dynamics"*, Universities Press, Hyderabad, 2004.

Sengupta, T.K., *"Instabilities of Flows and Transition to Turbulence"*, CRC Press, USA, 2012.

Sengupta, T.K., Bhaumik, S., "Onset of turbulence from the receptivity stage of fluid flows", Physical Review Letters vol. 107, 154501, 2011.

Sengupta, T.K., Bhumkar, Y., Lakshmanan, V., "Design and analysis of a new filter for LES and DES", Computers and Structures, vol. 87, pp.735–750, 2009.

Sengupta, T.K., Bhaumik, S., Singh, V., Shukl, S., "Nonlinear and nonparallel receptivity of zero-pressure gradient boundary layer", International Journal of Emerging Multidisciplinary Fluid Sciences vol. 1, pp.19–35, 2009a.

Sengupta, T.K., Bhumkar, Y., Rajpoot, M., Suman, V. K., Saurabh, S., "Spurious waves in discrete computation of wave phenomena and flow problems", Applied Mathematics and Computation, vol. 218, pp.9035-9065, 2012a.

Sengupta, T.K., De, S., Sarkar, S., "Vortex-induced instability of incompressible wall-bounded shear layer", Journal of Fluid Mechanics, vol. 493, pp.277–286, 2003.

Sengupta, T.K., Dipankar, A., "Sub-critical instability on the attachment of an infinite swept wing", Journal of Fluid Mechanics, vol. 529, pp.147–171, 2005.

Sengupta, T.K., Dipankar, A., Sagaut, P., "Error dynamics: Beyond von Neumann analysis", Journal of Computational Physics, vol. 226, pp.1211–1218, 2007.

Sengupta, T.K., Rajpoot, M K., Bhumkar, Y.G., "Space-time discretizing optimal DRP schemes for flow and wave propagation problems", Computers and Fluids, vol. 47, pp.144–154, 2011a.

Sengupta, T.K., Vijay, V.V.S.N., Bhaumik, S., "Further improvement and analysis of CCD scheme: dissipation discretization and de-aliasing properties", Journal of

Computational Physics, vol. 228, pp.6150–6168, 2009b.

Steger, J., Chaussee, D., "Generation of body-fitted coordinates using hyperbolic partial differential equations", SIAM Journal of Scientific and Statistical Computing, vol. 1, pp.431–437, 1980.

Tollmien, W., " Production of Turbulence", NACA Report-TM-609 (1931).

Vorst, H.A.V. der, "Bi-CGSTAB: A fast and smoothly converging variant of Bi-CG for the solution of non-symmetric linear systems", SIAM Journal of Scientific and Statistical Computing, vol. 13(2), pp.631–644, 1992.

Vichnevetsky, R., Bowles, J.B., *"Fourier Analysis of Numerical Approximations of Hyperbolic Equations"*, SIAM Studies in Applied Mathematics 5, Philadelphia, 1982.